

Molecular basis of the urate transporter URAT1 inhibition by gout drugs

Received: 10 September 2024

Accepted: 22 May 2025

Published online: 04 June 2025

 Check for updates

Yang Suo^{1,5}, Justin G. Fedor^{1,5}, Han Zhang², Kalina Tsoлова¹, Xiaoyu Shi³, Kedar Sharma⁴, Shweta Kumari², Mario Borgnia⁴, Peng Zhan³, Wonpil Im² & Seok-Yong Lee¹✉

Hyperuricemia is a condition when uric acid, a waste product of purine metabolism, accumulates in the blood. Untreated hyperuricemia can lead to crystal formation of monosodium urate in the joints, causing a painful inflammatory disease known as gout. These conditions are associated with many other diseases and affect a significant and increasing proportion of the population. The human urate transporter 1 (URAT1) is responsible for the reabsorption of ~90% of uric acid in the kidneys back into the blood, making it a primary target for treating hyperuricemia and gout. Despite decades of research and development, clinically available URAT1 inhibitors have limitations because the molecular basis of URAT1 inhibition by gout drugs remains unknown. Here we present cryo-electron microscopy structures of URAT1 alone and in complex with three clinically relevant inhibitors: benzbromarone, lesinurad, and the recently developed compound TD-3. Together with functional experiments and molecular dynamics simulations, we reveal that these inhibitors bind selectively to URAT1 in inward-open states. Furthermore, we discover differences in the inhibitor-dependent URAT1 conformations as well as interaction networks, which contribute to drug specificity. Our findings illuminate a general theme for URAT1 inhibition, paving the way for the design of next-generation URAT1 inhibitors in the treatment of gout and hyperuricemia.

Gout is a disease that afflicts up to 6.8% of the population globally¹ and is the most common form of inflammatory arthritis, particularly among men in developed countries^{1,2}. Characterized by recurrent episodes of acute inflammatory arthritis, gout is primarily driven by the deposition of monosodium urate crystals within joints. Hyperuricemia, a major risk factor for gout, is characterized by an accumulation of uric acid in the blood and is increasingly recognized as a potential contributor to a spectrum of comorbidities, including cardiovascular diseases, renal disorders, kidney failure, diabetes, and

metabolic syndrome³⁻⁸. Currently, 21% of Americans are diagnosed with hyperuricemia³, and global prevalence is estimated to be up to 36% in different populations⁴. Despite these implications, the management of hyperuricemia and gout remains suboptimal, largely due to limitations in current pharmacological interventions. Unfortunately, the number of gout cases is rapidly surging, with the prevalence of gout increasing globally from 1990 to 2019 by ~21%, and by 90.6% for men in the United States². This not only bears considerable impact on individual quality of life, but also a quickly growing burden for public

¹Department of Biochemistry, Duke University School of Medicine, Durham, NC, USA. ²Departments of Biological Sciences, Lehigh University, Bethlehem, PA, USA. ³Department of Medicinal Chemistry, Key Laboratory of Chemical Biology (Ministry of Education), School of Pharmaceutical Sciences, Cheeloo College of Medicine, Shandong University, Jinan, Shandong, P.R. China. ⁴Genome Integrity and Structural Biology Laboratory, National Institute of Environmental Health Sciences, National Institutes of Health, Department of Health and Human Services, Research Triangle Park, NC, USA. ⁵These authors contributed equally: Yang Suo, Justin G. Fedor. ✉e-mail: seok-yong.lee@duke.edu

health. Much-needed improvements in treatments are therefore needed through a better understanding of the causes of gout and the pharmacological targets.

The human urate transporter 1 (URAT1) is encoded by the *SLC22A12* gene, which belongs to the SLC22 family of organic cation/anion transporters. URAT1, primarily expressed on the luminal side of the renal proximal tubule, uptakes urate in exchange for exporting monocarboxylates⁹, serving as a specific and major regulator of uric acid reabsorption from the urine (Fig. 1a)^{9,10}. Approximately 90% of the urate filtered from the glomeruli is reabsorbed back to the bloodstream, while only 10% is excreted in the urine¹¹. Reabsorption of urate is largely mediated by URAT1, making it the critical target for the treatment of hyperuricemia and gout^{10–12}. Case in point, 90% of hypouricemia cases are linked to nonfunctional mutations in URAT1,

where the vast majority of mutations are protective against gout and hyperuricemia¹³. Inhibition of URAT1 is therefore an effective strategy to promote uric acid excretion to mitigate the risk of hyperuricemia-related complications, including gout¹¹.

Despite the clear therapeutic potential of targeting URAT1, the development of specific and potent inhibitors has proven challenging. Benzbromarone (BBR) has been used to treat gout for more than 30 years¹⁴. Although it is a potent inhibitor of URAT1 and effective at lowering serum uric acid concentrations, reports of hepatotoxicity have led to a reduction in its use^{15,16}. In 2015, the FDA approved lesinurad (LESU) as a recently developed inhibitor of URAT1 for the treatment of gout and hyperuricemia, but it must be co-administered with the xanthine oxidase inhibitor allopurinol due to its toxicity and low efficacy¹⁷. More recently, utilizing lesinurad as a lead compound, a

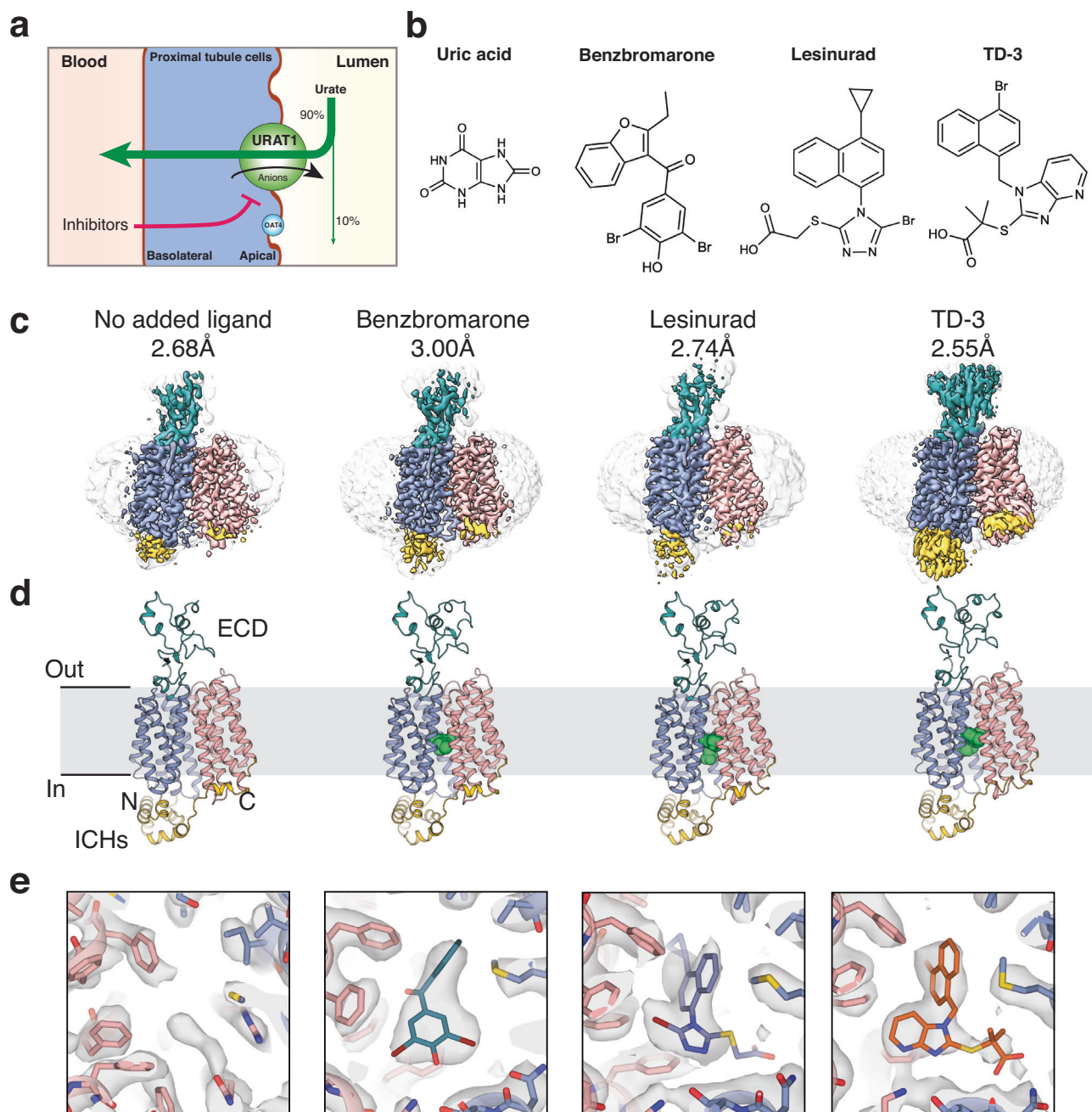


Fig. 1 | URAT1 biology and structure. **a** The role of URAT1 in urate reabsorption in the kidney proximal tubule epithelium. **b** Chemical structures of URAT1 substrate and inhibitors. **c–e** cryo-EM reconstructions, structures, and maps of the central

binding cavity for URAT1_{CS} alone and in complex with benzbromarone (BBR-URAT1_{CS}), lesinurad (LESU-URAT1_{CS}) and TD-3 (TD-3-URAT1_{CS}).

Table 1 | Cryo-EM data collection, refinement, and validation statistics

| | No ligand added-URAT1 _{CS} (EMD-46948) (PDB 9DK9) | BBR-URAT1 _{CS} (EMD-46949) (PDB 9DKA) | LESU-URAT1 _{CS} (EMD-46950) (PDB 9DKB) | TD-3-URAT1 _{CS} (EMD-46951) (PDB 9DKC) |
|---|--|--|---|---|
| <i>Data collection and processing</i> | | | | |
| Magnification | 105,000 | 105,000 | 105,000 | 105,000 |
| Voltage (kV) | 300 | 300 | 300 | 300 |
| Electron exposure (e ⁻ /Å ²) | 50 | 50 | 45 | 60 |
| Defocus range (μm) | -0.8 to -1.8 | -0.8 to -1.8 | -0.8 to -1.8 | -1.0 to -2.0 |
| Pixel size (Å) | 0.835 | 0.855 | 0.4128 | 0.8469 |
| Symmetry imposed | C1 | C1 | C1 | C1 |
| Initial particle images (no.) | 6,980,323 | 7,735,079 | 9,515,658 | 1,954,727 |
| Final particle images (no.) | 527,705 | 220,530 | 512,313 | 505,707 |
| Map resolution (Å) | 2.68 | 3.00 | 2.74 | 2.55 |
| FSC threshold | 0.143 | 0.143 | 0.143 | 0.143 |
| Map resolution range (Å) | 2.56–33.77 | 2.75–7.11 | 2.71–4.66 | 2.52–6.36 |
| <i>Refinement</i> | | | | |
| Initial model used (PDB code) | TD-3-URAT1 _{CS} | TD-3-URAT1 _{CS} | TD-3-URAT1 _{CS} | 8ET6 |
| Map sharpening B factor (Å ²) | -123.3 | -137.65 | -146.7 | -104.6 |
| <i>Model composition</i> | | | | |
| Non-hydrogen atoms | 7660 | 7738 | 7662 | 7708 |
| Protein residues | 517 | 517 | 517 | 517 |
| Ligands | 0 | BNZ:1 | LES:1 | TD-3:1 |
| <i>B factors (Å²)</i> | | | | |
| Protein | 66.21 | 65.74 | 80.96 | 113. |
| Ligand | - | 30.00 | 85.33 | 93.91 |
| <i>R.m.s. deviations</i> | | | | |
| Bond lengths (Å) | 0.003 | 0.003 | 0.003 | 0.006 |
| Bond angles (°) | 0.557 | 0.684 | 0.610 | 0.715 |
| <i>Validation</i> | | | | |
| MolProbity score | 1.30 | 1.31 | 1.34 | 1.33 |
| Clashscore | 5.61 | 5.70 | 6.14 | 4.67 |
| Poor rotamers (%) | 0.78 | 0.52 | 0.00 | 0.52 |
| <i>Ramachandran plot</i> | | | | |
| Favored (%) | 98.83 | 98.25 | 98.45 | 98.25 |
| Allowed (%) | 1.17 | 1.75 | 1.55 | 1.75 |
| Disallowed (%) | 0.00 | 0.00 | 0.00 | 0.00 |

group of bicyclic imidazopyridines were developed as URAT1 inhibitors¹⁸. Among these, a compound named TD-3 (compound **23** in the original study) exhibits exceptional properties, including excellent ability to lower serum urate in vivo, favorable safety and pharmacokinetic properties, oral bioavailability, and potent in vitro inhibition (IC₅₀ 1.36 μM), surpassing lesinurad in all aspects¹⁸. Overall, TD-3 shows promise as a drug candidate for hyperuricemia and gout¹⁸.

These issues and progress highlight the pressing need for the development of more selective and safer URAT1 inhibitors. In this work, we seek to better understand URAT1 inhibition through functional assays and cryo-EM, focusing on the inhibitors BBR, LESU and TD-3. Our aim is to identify key structural features of URAT1 that could be leveraged for future drug development.

Results

URAT1_{CS} binds inhibitors in the inward-open conformation

Wild-type human URAT1 exhibits poor expression and stability when expressed in HEK293S GnT1⁻ cells, hindering structural elucidation. We turned to consensus mutagenesis to improve protein yield and stability, as previously implemented in our laboratory¹⁹. We obtained a construct with 100% sequence identity to human URAT1 in the central

ligand binding cavity, with an overall 91% sequence identity to human URAT1 (Supplementary Fig. 1a, 11). We hereafter refer to this construct as URAT1_{CS}, which shows superior expression yields and stability by size-exclusion chromatography (Supplementary Fig. 1b). However, [¹⁴C]-uric acid (UA) uptake assays in HEK293T cells transiently expressing hURAT1 and URAT1_{CS} show that URAT1_{CS} has substantially weaker uptake activity compared with hURAT1 (Supplementary Fig. 1c), albeit with significantly higher surface expression (Supplementary Fig. 1d). This suggests URAT1_{CS} adopts an over-stabilized conformation but is still capable of turnover. Importantly, measurement of the IC₅₀ for BBR, LESU and TD-3 in HEK293T cells expressing hURAT1 versus URAT1_{CS} shows that URAT1_{CS} binds these inhibitors with high affinity (Supplementary Fig. 1e–g). So, despite a very slow turnover, the inhibitor binding site and properties of the central cavity are preserved.

We determined the cryo-electron microscopy (cryo-EM) structures of URAT1_{CS} alone at 2.68 Å, in complex with benzbromarone (BBR-URAT1_{CS}) at 3.00 Å, in complex with lesinurad (LESU-URAT1_{CS}) at 2.74 Å and in complex with TD-3 (TD-3-URAT1_{CS}) at 2.55 Å (Fig. 1c, d, Supplementary Figs. 2 and 3, Table 1). Robust cryo-EM densities within the central cavity were identified, and the corresponding inhibitors

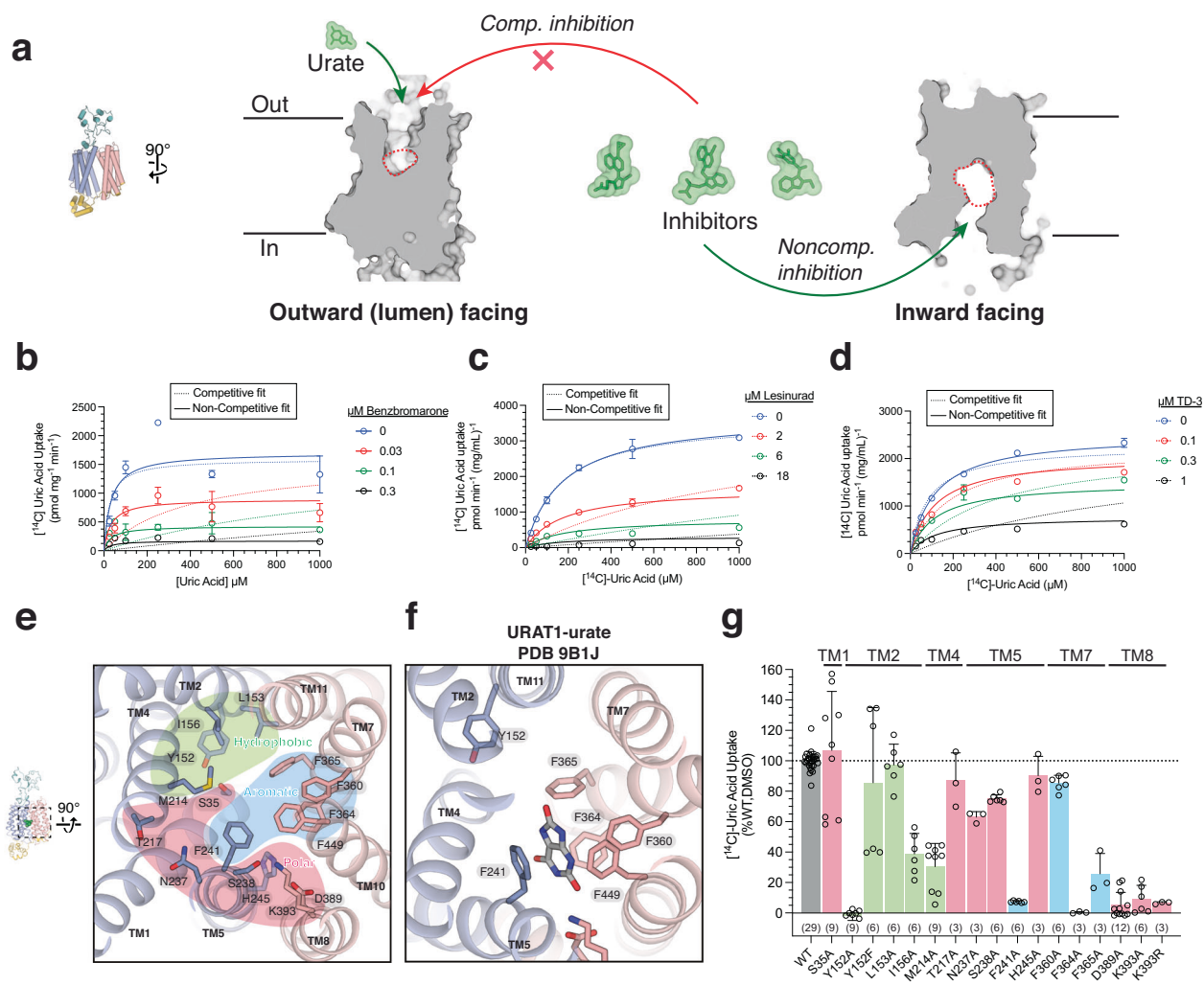


Fig. 2 | URAT1 inhibitors bind non-competitively to the inward-open conformation. **a** Comparing the inward-facing (this study) and outward-facing (PDB 8WJQ²⁵) URAT1 central cavity size highlights the steric restriction for inhibitor binding to the outward-facing conformation of URAT1, demonstrating the possible modes of inhibition. **b–d** Inhibition kinetics determination of $[^{14}\text{C}]$ -urate uptake (0.9 Ci/mol) for BBR, LESU and TD-3, respectively, demonstrating that all three inhibitors inhibit URAT1 non-competitively. Data are presented as mean \pm standard error of the mean (S.E.M.) ($n = 3$ biological replicates) with global non-linear fits for

non-competitive (solid lines) or competitive (dashed lines) models of inhibition. Best fit values and fitting statistics are provided in Table 2. **e** Central cavity of URAT1, using no ligand added URAT1_{CS}. **f** Binding mode of urate within the central cavity of inward-open URAT1 using PDB 9B1J²³, highlighting the role of the aromatic clamp and hydrophobic region of the cavity. **g** Effects of mutations on the central binding cavity residues on uptake of 200 μM $[^{14}\text{C}]$ -urate (0.9 Ci/mol) in HEK293T cells for 10 min at 37 °C in the presence of 1% DMSO. Data presented as mean \pm standard deviation (S.D.) ($n = 3$ –29 biological replicates).

were unambiguously modeled. There is also a weaker density in the central cavity of URAT1_{CS} alone, likely from an endogenous molecule, but its position and shape are distinct from those of the inhibitors (Fig. 1e, Supplementary Fig. 4).

Like previously published OCT and OAT structures^{19–22}, URAT1 adopts a major facilitator superfamily (MFS) fold that consists of an extended extracellular domain (ECD), a 12-helical transmembrane domain (TM) and an intracellular helical bundle (ICH). The TM bundle forms a 6 + 6 pseudosymmetrical arrangement where TMs 1–6 form the N-terminal lobe (N-lobe), and TMs 7–12 comprise the C-terminal lobe (C-lobe).

Interestingly, all the structures we report are of the inward-open conformation, evidenced by the large opening of the central cavity to the intracellular side (Fig. 1d). All the inhibitors occupy the central binding pocket and make extensive interactions with URAT1_{CS}, suggesting inhibitors may prefer to bind to the inward-facing states (Fig. 1e). Recently published structures of URAT1 with inhibitors bound also show these compounds bind to the central cavity of the inward-facing conformation²³. No structure of inhibitor-bound

URAT1 in the outward-facing conformation has been reported, although uric acid binds to multiple conformations²³. This is notable given that the common mechanism of clinical transporter inhibitors is to stabilize outward-facing conformations^{19,24–27}. We therefore sought to explore the functional implications of this mode of binding to URAT1.

URAT1 drugs are non-competitive inhibitors of uric acid uptake

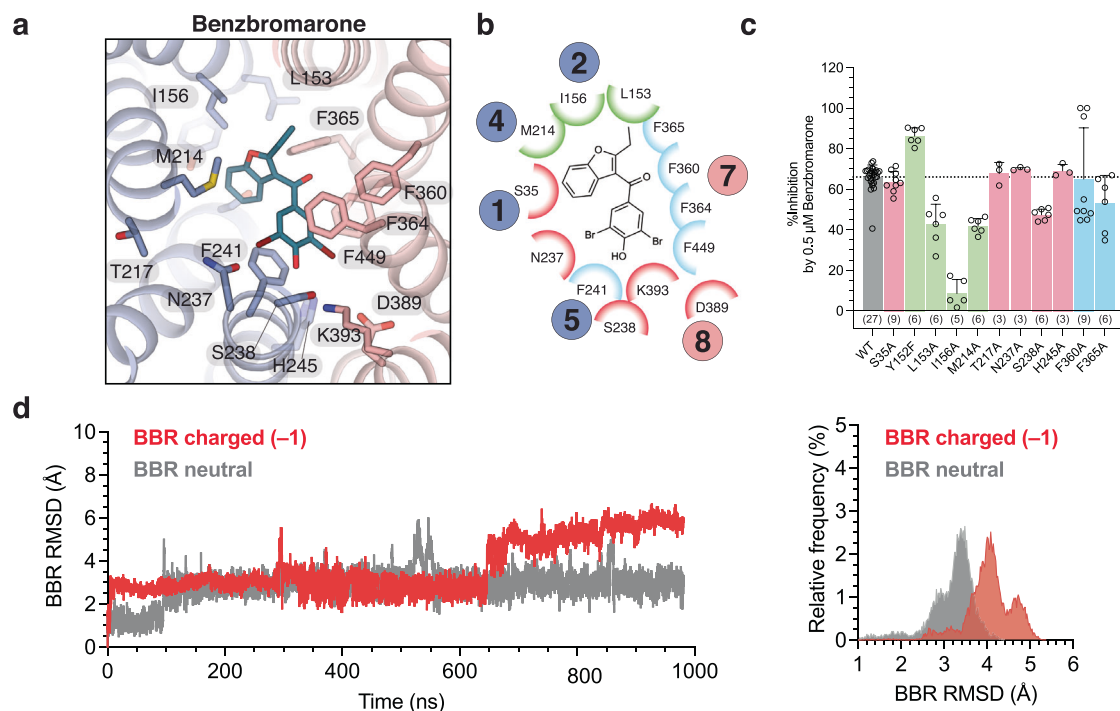
We conducted a series of uptake experiments in HEK293T cells transiently transfected with hURAT1, where $[^{14}\text{C}]$ -uric acid and inhibitor are introduced outside the cells, and their concentrations were varied to establish the mode of inhibition for each of the compounds tested. We predicted that since the inhibitors occupy the same central binding pocket as uric acid, inhibitors stabilizing outward-facing states will exhibit competitive inhibition whereas those stabilizing inward-facing states will exhibit non-competitive inhibition (Fig. 2a). We found that when comparing non-linear fits to the data of competitive versus non-competitive inhibition, the non-competitive models consistently resulted in far superior fits (Fig. 2b–d, Table 2). The functional data are

Table 2 | Inhibition kinetics model fitting parameters

| Inhibitor | Kinetic model | K_T urate (μM) ^a | K_i (μM) ^a | V_{max} ($\text{pmol min}^{-1} \text{mg}^{-1}$) ^a | $Sy.x$ ^b |
|-----------|-----------------|--|--------------------------------------|---|---------------------|
| BBR | Competitive | 26.08 [11.29–48.59] | 0.00213 [0.001–0.0042] | 1591 [1355–1846] | 306.7 |
| | Non-competitive | 32.4 [20.7–47.9] | 0.033 [0.025–0.045] | 1700 [1530–1881] | 231.0 |
| LESU | Competitive | 162.8 [126.4–210.1] | 0.348 [0.275–0.439] | 3625 [3335–3955] | 196.3 |
| | Non-competitive | 175.1 [148.8–206.5] | 1.63 [1.46–1.82] | 3725 [3522–3947] | 137.2 |
| TD-3 | Competitive | 82.19 [59.19–113.0] | 0.079 [0.057–0.111] | 2259 [2071–2472] | 208.0 |
| | Non-competitive | 115.3 [99.21–130.4] | 0.44 [0.38–0.50] | 2515 [2393–2644] | 122.1 |

^aFit value with 95% confidence interval [lower value–upper value].

^bModel fit quality as reported by the standard deviation of the residuals, where $Sy.x = \sqrt{\frac{\sum(\text{residual}^2)}{n-k}}$ and n is the number of data points (18) and k is the number of fitting parameters (3). When comparing two models, a lower value denotes a better fit. For all inhibitors tested, non-competitive models yield superior fits.

**Fig. 3 | URAT1 central cavity and benzbromarone binding site interactions.**

a, b Binding interactions with BBR. **c** Effects of mutations on inhibition by 0.5 μM BBR on uptake of 200 μM [^{14}C]-urate (0.9 Ci/mol) in HEK293T cells for 10 min at 37 °C. Data reported as mean \pm S.D. for $n = 3$ –27 biological replicates. **d** Left,

representative time series traces of root mean squared deviation (R.M.S.D) for charged (red) or neutral (gray) BBR binding in a 1 μs MD simulation. Right, frequency distribution of R.M.S.D. values for charged (red) or neutral (gray) BBR binding over all five replicate MD simulations.

consistent with our structural observations that these inhibitors stabilize inward-facing states of URAT1.

Structures of URAT1 (apo and with uric acid bound) in the outward-open conformation were recently reported^{23,28} of constructs that either utilized the R477S mutation²⁸ or a combination of loop engineering and maltose binding protein (MBP)-designed ankyrin repeat protein (DARPin) fusions²³. Comparing the binding site of the inward- and outward-open conformations of URAT1 reveals that the cavity is far too restrictive in the outward-open conformation to allow inhibitor binding, while the inward-open conformation is much more expansive (Fig. 2e), likely explaining why there are no reported inhibitor-bound structures of outward-open URAT1²⁸.

The fact that many MFS transporters bind inhibitors in the outward open state is functionally consistent with inhibitors most commonly accessing the transporter from the cell exterior (i.e. blood) to inhibit transport. URAT1 is expressed on the apical membrane in the proximal tubule of kidneys, so URAT1 is exposed to the urine but not to the blood (Fig. 1a). We therefore propose that URAT1 inhibitors bind non-competitively from the intracellular side of the apical membrane

(Figs. 1a and 2a). We then wanted to investigate the binding site and probe the functional significance of the residues lining it.

Central cavity of URAT1

In the URAT1_{CS} structure, the central cavity is mildly conserved (Supplementary Fig. 5) and lined with amino acid residues that can be divided into three general groups: a cluster of hydrophobic residues that are distributed on TM2 and TM4 including Y152, L153, I156 and M214, which we termed the hydrophobic region; a cluster of aromatic residues on TM5, TM7 and TM10 that spans two opposite sides of the cavity including F241, F360, F364, F365 and F449, which we term the aromatic clamp; and a span of polar or charged residues on TM1, TM4, TM5, and TM8 including S35, T217, N237, S238, D389 and K393 (Fig. 3a). In most MFS-type transporters, TMs 1, 4, 7 and 10 (termed as A helices) form the central substrate-binding cavity²⁹. In contrast, TMs 1, 2, 4, 5, 7, 8 and 10 are all involved in the formation of the central binding cavity of URAT1_{CS} in an inward-facing state. This recruitment of additional TMs is an intriguingly distinct mechanism for URAT1 substrate/inhibitor recognition and function.

We performed mutagenesis together with radioactive uptake of [^{14}C]-uric acid and found that the aromatic and hydrophobic residues on TMs 2 and 7 (Y152, I156, M214, F364, F365) exhibit great effects on uric acid uptake upon mutation (Fig. 3b). Notably, F364A abolishes function despite its surface expression (Supplementary Fig. 6). D389 and K393 on TM8 form a salt bridge that is likely more critical to transporter gating than substrate binding directly, as they do not appear close enough to directly interact with uric acid, in agreement with the previous structure²⁸. Interestingly, K393 is critical for function, as K393R does not substantially restore activity compared to K393A. Of the critical residues, Y152A is not expressed (Supplementary Fig. 6), but Y152F largely restores activity (Fig. 3b).

Binding of benzbromarone to URAT1

In our structure of BBR-URAT1_{CS} there is an unambiguous non-protein cryo-EM density centered within the cavity, which allowed us to build the BBR molecule with good confidence, and its conformation is similar to published BBR structures (Supplementary Fig. 7a). BBR forms extensive interactions with the aromatic clamp and occupies the hydrophobic region with its benzofuran group, a position occupied by uric acid in the outward-open conformation²⁸ (Supplementary Fig. 8). Interestingly, the brominated phenolic group interacts with F364 as well as F241 and F449 of the aromatic clamp via π - π interactions. F241 and F364 are both required for uric acid transport as their mutation to alanine eliminates activity, therefore the effect of these mutations on inhibitor binding could not be probed by activity assays (Fig. 2g). The F365A mutant also significantly reduces activity (-25% WT; Fig. 2g), but has a rather minimal impact on BBR binding, interacting only slightly with the benzofuran group (Fig. 3a–c). L153A, I156A and M214A, however, have larger effects on inhibition potency, and S238 on TM5 also shows an effect, indicating an important role for these residues for inhibition and a particular importance of the hydrophobic region for BBR binding. To verify the binding mode and stability of BBR binding, molecular dynamics (MD) simulations were conducted on both the charged and neutral forms of BBR, where ionization of the phenolic hydroxyl is readily delocalized across the phenolic ring and extends to the para-carbonyl (Supplementary Fig. 7b)³⁰. Benzbromarone appears additionally stabilized by interactions of the partially ionized hydroxyl with K393 (Fig. 3a, b), which is absolutely required for transporter function, so its contribution to benzbromarone binding affinity could not be elucidated (Fig. 2g). The MD results in Fig. 3d show the representative R.M.S.D trajectory and histogram for the anionic and neutral forms of BBR within a 1 μs timespan, respectively (Supplementary Fig. 9). Neutral BBR, having a lower average R.M.S.D, appears to be more stable inside the cavity compared to the anionic form. This suggests a possible charge interaction with K393 does not significantly contribute to BBR binding, and the neutral form of BBR is more stably bound to URAT1 than the anionic form.

Inhibition of URAT1 by lesinurad and TD-3

LESU and TD-3 were modeled confidently into strong, unambiguous densities within the central cavity of URAT1_{CS} (Fig. 1e). We noticed that the binding pose of our LESU is distinct from those of recently reported structures^{23,31} (Supplementary Fig. 10). We therefore made careful analyses including map-to-model correlations, all-atom MD simulations, and visual inspection and concluded that our LESU binding pose is the most accurate model (Supplementary Fig. 10). For both LESU and TD-3 the naphthalene ring (including the bromo/cyclopropyl groups of LESU/TD-3, respectively) largely occupies the hydrophobic region, whereas the heterocycle moieties interact with the aromatic clamp (Fig. 4a, b, d, e). Within the hydrophobic region, M214A has the largest impact on inhibition by LESU (Fig. 4c) and TD-3 (Fig. 4f), in comparison to BBR where I156 plays a more significant role in binding (Fig. 3c). M214 interacts broadly with LESU and TD-3 and specifically with the naphthalene rings of both through an S- π

interaction, which is known to impart significant binding stabilization^{32,33}. Unlike BBR, LESU and TD-3 contain mono-carboxylates—localized anions—like the endogenous counter substrates of URAT1⁹. However, while K393 appears to electrostatically stabilize BBR binding, the carboxylates of LESU and TD-3 bind away from K393, appearing instead to potentially hydrogen bond with N237. Mutation of N237 to alanine does not, however, appreciably impact inhibition potency (Fig. 4c, f). M214 also engages with the carboxylate arms of LESU and TD-3. Our MD simulations show stable binding of both drugs (Fig. 4g, h) regardless of charge state (Supplementary Fig. 9), but TD-3 shows less mobility within the cavity compared to LESU, which may correlate with its higher affinity to hURAT1. Specifically, the carboxylates of both LESU and TD-3 show considerable rotatability during MD simulations, with the carboxyl and dimethyl groups of the carboxylate arm of TD-3 appearing to always interact with M214. A residue that again demonstrates its importance is S238 on TM5, which appears to hydrogen bond with the heterocyclic triazole and imidazo-pyridine rings of LESU and TD-3, which are sandwiched by the aromatic clamp. Mutation of S238 to alanine substantially reduces the inhibition potency of TD-3, and to a lesser extent, LESU. A picture therefore emerges that rather than highly specific salt bridge interactions between URAT1 and its inhibitors, there is a structural, electrostatic and hydrophobic complementarity with π - π interactions provided by the aromatic clamp, S- π interactions from M214, a general electro-positive environment (Fig. 5b) and potential water-mediated interactions with S238 on TM5. Notably, based on the structure of urate-bound URAT1, urate overlaps perpendicularly with the location of the naphthalene ring of the inhibitors (Supplementary Fig. 8). The larger size, electronegativity, and hydrophobicity of the inhibitors are critical for their high-affinity binding and ability to lock the transporter in the inward-open conformation. Therefore, the interactions mediated by the aromatic clamp and the polar group (both involving TMs) are important for activity and inhibitor binding.

Conformational flexibilities upon inhibitor binding

Despite all our URAT1_{CS} structures being inward-open, directly overlaying the models reveals an -10° bend in TM5 of the TD-3-URAT1_{CS} structure, relative to the LESU- and BBR-URAT1_{CS} structures (Fig. 5a). TM5 of URAT1_{CS} alone adopt a conformation similar to that of TD-3 bound URAT1_{CS}, likely due to the endogenous molecule bound to the URAT1_{CS} in the absence of inhibitors (Supplementary Fig. 4a). This bend in TM5 originates at G240, in proximity to the previously mentioned S238 residue that is important for inhibitor binding. Importantly, this conformational change is required to accommodate TD-3, where a clash between TD-3 and N237 occurs with the LESU-bound conformation. This observation suggests that there is a conformational ensemble defined by the position of TM5, which can determine inhibitor specificity. Furthermore, unlike for other organic anion/cation transporters, there is no direct specific interaction of the charged substrate/drug moiety with a complementary charged residue^{19,20}. While R477 may have a role, the distance between the guanidinium and the charged moieties of these inhibitors is $>9 \text{ \AA}$. The other basic residue, K393 interacts with the phenolic oxygen of BBR, but is $\geq 8 \text{ \AA}$ from the carboxylates of LESU and TD-3. A view of the electrostatics of the URAT1_{CS} cavity shows, however, that the region to which these carboxylate moieties or the phenolic ring of BBR occupy is generally electropositive (Fig. 5b). Interestingly, the subtle conformational shift of TM5 in the TD-3 structure induces an electrostatic change in the upper portion of the cavity, which also appears to open slightly larger for solvent access, suggesting that the conformational difference is not limited to TM5 rotation.

Discussion

Taken together, utilizing cryo-EM, functional studies and MDs simulations, we have elucidated the inhibitory mechanism of URAT1 by

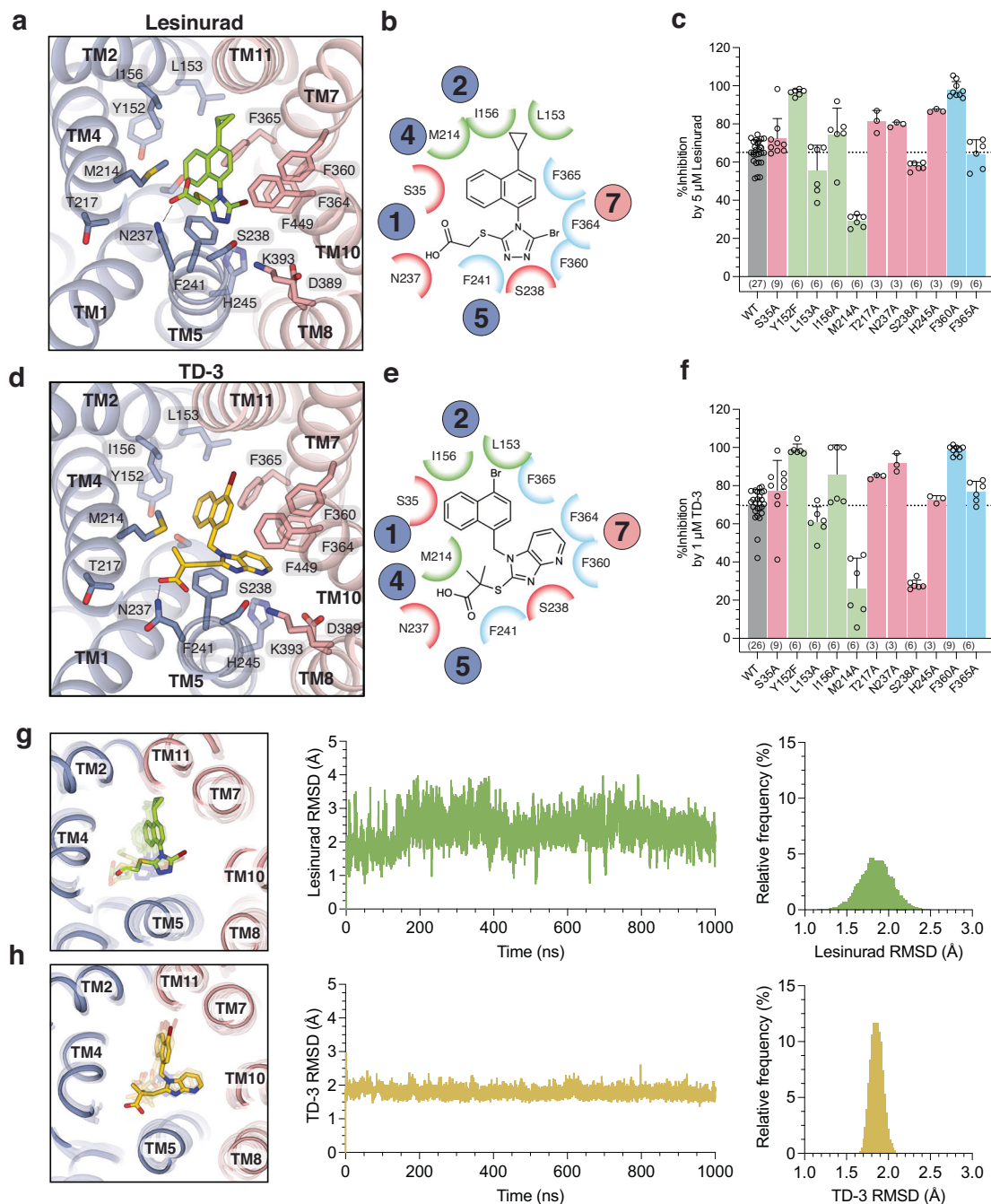


Fig. 4 | Lesinurad and TD-3 binding site interactions. a, b Binding interactions with LESU. **c** Effects of mutations on inhibition by 5 μM LESU on uptake of 200 μM [¹⁴C]-urate (0.9 Ci/mol) in HEK293T cells for 10 min at 37 °C. Data reported as mean ± standard deviation (S.D.) for $n = 3-27$ biological replicates. **d, e** Binding interactions with TD-3. **f** Effects of mutations on inhibition by 1 μM TD-3 on uptake of 200 μM [¹⁴C]-urate (0.9 Ci/mol) in HEK293T cells for 10 min at 37 °C. Data

reported as mean ± standard deviation (S.D.) for $n = 3-26$ biological replicates.

g, h Left, Comparison of cryo-EM structure (no transparency) and MD simulation snapshots (with transparency) of anionic LESU and TD-3 binding to URAT1. Middle, representative R.M.S.D. time series trace of LESU and TD-3 binding in 1 μs MD simulations. Right, frequency distribution of R.M.S.D. values for LESU and TD-3 binding, respectively, over all five replicate MD simulations.

three clinically relevant inhibitors, revealing critical details about their binding poses and the conformational changes upon binding, as summarized in Fig. 5c, d. URAT1 is a specific transporter for uric acid, but in exchange transports a variety of mono-carboxylates which have a defined negative charge but vary in size⁹. URAT1, in the outward-open conformation, forms a small pocket complementary to uric acid binding from the kidney lumen. Upon changing conformation to the inward-open state, the binding pocket expands into a large electro-positive cavity, expelling uric acid and allowing counter substrate binding. Specifically, the aromatic clamp formed by F241 and F449 is

closed in the outward-open conformation but opens in the inward-open conformation (Fig. 5c)²³. This poses an excellent opportunity for inhibitors to bind to the large, hydrophobic yet electro-positive cavity of the inward-open URAT1, stabilized by the aromatic clamp, giving rise to a rather unique non-competitive mode of inhibition. Most inhibitory drugs that target transporters, particularly MFS transporters, lock or stabilize the outward-facing conformation^{19,24-27}. Several inhibitor drugs have been found to bind to inward-facing conformations, but this is mostly a feature of the neurotransmitter/sodium symporter family of transporters^{25,26,34}. Our data suggest that most

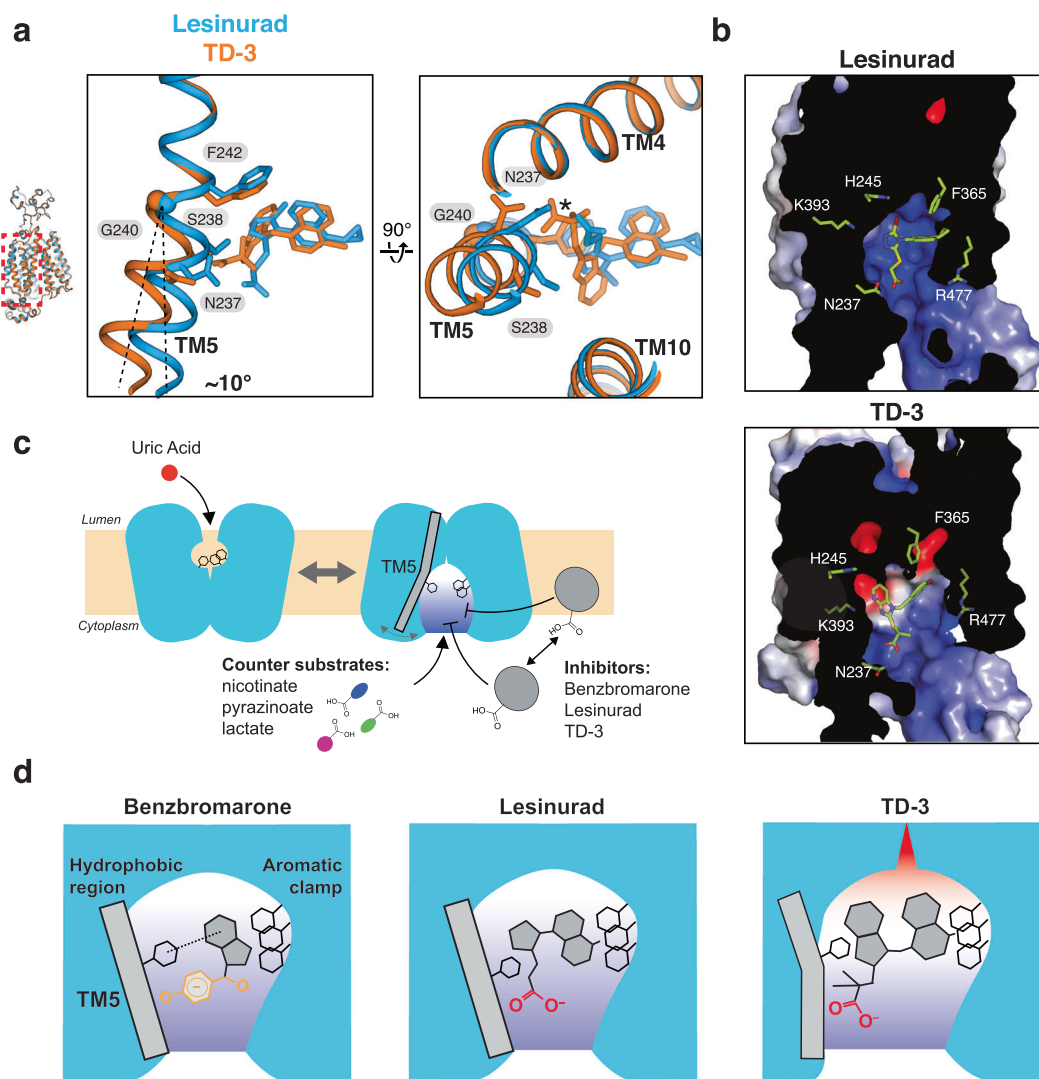


Fig. 5 | TM5 mobility and binding model for URAT1 inhibitors. **a** Conformational changes between Les-URAT1_{CS} and TD-3-URAT1_{CS}, highlighting TM5 and relevant residues. Note the potential steric clash (*) between lesinurad and N237 in TD-3-URAT1_{CS}. **b** Electrostatic potential surface in Les-URAT1_{CS} (top) and TD-3-URAT1_{CS}

(bottom), respectively. **c** Proposed model for URAT1 substrate transport and inhibition. **d** Proposed mode for differential inhibition potency among BBR, LESU and TD-3.

URAT1 inhibitors, if not all, likely target the inward-facing states of URAT1. Consistent with this idea, most URAT1 inhibitors are hydrophobic anions that can partition into and pass through the basolateral side of the membrane from the blood, gaining access to URAT1. We posit that this is the optimal strategy for inhibiting not only URAT1, but also other uptake transporters located on the luminal face of the epithelium, like in the gut and kidney.

The variability observed in drug-bound TM5 conformation suggests that multiple sub-conformations of the inward-open state are possible, which may provide greater flexibility in accommodating various anionic counter substrates. This is particularly valuable considering that, without this subtle conformational change, TD-3 cannot bind to URAT1 and that this change drastically modifies the upper cavity electrostatics, opening novel sites for inhibitor interaction. It is unclear whether an induced-fit or conformation-selective mechanism is employed in inhibitor binding to URAT1. Given that variously sized monocarboxylates act as counter anions, and that many natural URAT1 inhibitors exist—including multicyclic terpenes and long chain polyunsaturated fatty acids, which range significantly in size¹²—we speculate that inhibitors bind to URAT1 via a conformation selection mechanism. The energetic penalty for switching to an inhibitor-

specific conformation would therefore play a role in inhibitor specificity^{35,36}. This feature can be leveraged to achieve greater specificity and efficacy in transporter-targeted drug design.

We acknowledge a limitation of our study is the use of a consensus construct (Supplementary Fig. 1a), which greatly facilitated our structural studies by being highly stabilized in the inward-open conformation albeit with substantially compromised activity (Supplementary Fig. 1c). Most importantly the structure is nearly identical to other published structures, with C α RMSD values ≤ 1 Å (Supplementary Fig. 10b), and allowed us to determine the highest resolution structures and most accurate ligand binding poses (Supplementary Fig. 10a). We therefore believe that this strategy remains a valuable tool for structural elucidation of other dynamic and less stable proteins.

Our structural, computational, and functional analyses reveal features critical for inhibitor binding. We found that the interactions of the heterocycle and carboxylate groups of the inhibitors with the aromatic clamp and the polar group (both involving TM5) are particularly important. The stronger interactions at these regions make TD-3 a higher-affinity inhibitor than LESU. It also does not seem that there is a critical basic residue responsible for stabilization of the anionic

inhibitors, but that these compounds bind to a generally electro-positive cavity, where residues like K393 and R477 contribute. This appears to be the general case for the SLC22 family of transporters, which tend to lack a single defined critical charged residue that stabilizes the complementarily charged ligand^{19,22}. Further structure-guided optimization of these interactions will be crucial in developing the next generation of URAT1 inhibitors.

Our findings also suggest that the hydrophobic nature of URAT1 inhibitors not only facilitates interactions with the hydrophobic region of the cavity but also increase their effective local concentrations by partitioning into the membrane³⁷, contributing to their apparent affinities. BBR has the greatest apparent affinity and, in the neutral form, has the highest predicted partition coefficient (XLogP3 = 5.7), whereas LESU is less hydrophobic (XlogP3 = 4.7)³⁸ and appears to bind less tightly. This difference is expected to be exacerbated for the charged states, where the negative charge on BBR is distributed over the entire phenolic system and carbonyl oxygen (Supplementary Fig. 7b) but concentrated on the carboxylate of LESU and TD-3. High hydrophobicity of BBR would increase its effective concentration substantially, whereas anionic LESU does less well. Consistent with this idea, the MD simulations of BBR binding suggest that direct interactions between BBR and URAT1 are weaker than those of LESU and TD-3. The high hydrophobicity and delocalized negative charge make BBR likely to interact with many off-target membrane proteins, as already reported in its effects on many different classes of membrane and soluble proteins^{39–45}. TD-3 has a moderate partitioning but stronger interactions with URAT1 compared to LESU, which results in superior pharmacology, suggesting that a tuning of compound hydrophobicity is required for optimal drug targeting. These differences in charge density and binding may also contribute to drug specificity, as LESU and TD-3 are able to bind with their carboxylates more deeply into the electropositive portion of the cavity. Tailoring carboxylate positioning to perhaps better engage K393 and/or R477, as well as tuning interactions with key residues like M214 and S238, could also be considered for future therapeutic development. This, in addition to ensuring compound hydrophobicity for lipid partitioning, ensures that drug binding engages both the N- and C-domains of the transporter by utilizing the aromatic clamp and hydrophobic region to rigidly stabilize the inward-open conformation of the transporter.

The rising global incidence and suffering caused by gout and hyperuricemia, and the increasing burden on public health systems, necessitates the development of novel inhibitors of URAT1 that exploit the features outlined above. We believe the insights provided by our studies can help achieve more optimal drugs to combat this growing issue.

Methods

Consensus mutagenesis design

Consensus constructs were designed in a similar manner to what has been previously reported^{19,27}, with minor modifications. First, PSI-BLAST was performed to identify 250 hits from UniProt database using human wild-type URAT1 (UniProt ID Q96S37) as query. The hits were manually curated to remove non-URAT1 or incomplete sequences. The remaining sequences were subjected to sequence alignment using MAFFT⁴⁶. The consensus sequence was then extracted in JalView⁴⁷ and aligned to the WT sequence in MAFFT. The final construct features sequence registers consistent with WT.

HEK293T radiotracer uptake assays

HEK293T cells (ATCC) were cultured in DMEM media (Gibco) supplemented with 10% (v/v) FBS (Gibco) and penicillin-streptomycin (Gibco). The full-length human URAT1 or URAT_{CS} sequences were codon-optimized for *Homo sapiens* and cloned into the BacMam vector with a PreScission protease-cleavable C-terminal green fluorescent protein (mEGFP) and FLAG-10xHis purification tags. Site-

directed mutagenesis was used to introduce mutations into this background. Empty vector controls utilize the BacMam vector bearing only a FLAG-10xHis-tagged mEGFP. Cells were grown to 60–80% confluency in 10 cm dishes and transfected using 7 µg plasmid DNA and 7 µL TransIT-Pro reagent (Mirus Bio). The next day, cells were detached and transferred to poly-L-lysine-treated 24-well plates. After an additional two days at 37 °C, the wells were rinsed three times with uptake buffer (25 mM MES-NaOH (pH 5.5), 125 mM Na⁺-gluconate, 4.8 mM K⁺-gluconate, 1.2 mM MgSO₄, 1.2 mM KH₂PO₄, 5.6 mM glucose, 1.3 mM Ca²⁺-gluconate)⁴⁸ and incubated at 37 °C for 15 min. Uptake was initiated by replacing the media with pre-warmed uptake buffer containing the respective concentrations of [¹⁴C]-uric acid (Moravek) and inhibitors. Uptake was quenched by addition of ice-cold DPBS (+Ca²⁺/Mg²⁺), then washed thrice with ice-cold DPBS (+Ca²⁺/Mg²⁺). Cells were lysed in 0.1M NaOH, the protein concentration determined by bicinchoninic acid (BCA) assay, and then transferred to scintillation vials containing EcoLumeTM (MP Biomedicals) for counting or mixed with Ultima Gold XR and subjected to scintillation counting using a MicroBeta2.

For inhibition kinetics studies, data were fit using GraphPad Prism using competitive (Eq. 1) or non-competitive (Eq. 2) fitting models⁴⁹, where K_T is the transport equivalent of the Michaelis constant (K_M), V_{max} is the maximal rate of transport, and K_I is the equilibrium constant for inhibitor binding.

Competitive inhibition:

$$v = \frac{V_{max}[S]}{K_T^{app} + [S]} \quad (1)$$

Non-competitive inhibition:

$$v = \frac{V_{max}^{app}[S]}{K_T + [S]} \quad (2)$$

Where $K_T^{app} = K_T \left(1 + \frac{[I]}{K_I}\right)$ and $V_{max}^{app} = V_{max} / \left(1 + \frac{[I]}{K_I}\right)$

Confocal microscopy of URAT1-expressing cells

Confocal microscopy confirming surface expression of URAT1 and mutants is performed as follows. HEK293T cells were transiently transfected with the same construct used for uptake assays. After seeding to glass bottom plates and allowing 2–3 days of expression, cells are washed with DPBS two times, followed by nucleus staining with 10 µM Hoechst 33342 (ThermoFisher) for 10 min. Cells were then washed three times with DPBS and subjected to confocal imaging using 405 nm (Hoechst 33342) and 488 nm (GFP) channels, respectively, using a Nikon AX confocal microscope equipped with a ×20 objective lens.

URAT1 protein expression and purification

Full-length consensus URAT1 sequences were codon-optimized for *Homo sapiens* and cloned into the Bacmam vector, in-frame with a PreScission protease cleavage site, followed by EGFP, FLAG-tag and 10× His-tag at the C-terminus. Baculovirus was generated according to manufacturer's protocol and amplified to P3. For protein expression, HEK293S GnTI⁻ cells (ATCC) were cultured in Freestyle 293 media (Life Technologies) supplemented with 2% (v/v) FBS (Gibco) and 0.5% (v/v) Anti-Anti (Gibco). Cells were infected with 2.5% (v/v) P3 baculovirus at $2.5\text{--}3 \times 10^6 \text{ ml}^{-1}$ cell density. After 20 h of shaking incubation at 37 °C in the presence of 8% CO₂, 10 mM sodium butyrate (Sigma-Aldrich) was added to the cell culture and the incubation temperature was lowered to 30 °C to boost protein expression. After 40–44 h, the cells were harvested by centrifugation at 550 ×g, and was subsequently resuspended with lysis buffer (20 mM Tris pH 8, 150 mM NaCl, 10 µg mL⁻¹ leupeptin, 10 µg mL⁻¹ pepstatin, 10 µg mL⁻¹ aprotinin, 1 mM phenylmethylsulphonyl fluoride (PMSF, Sigma-Aldrich). The cells were

lysed by probe sonication (30 pulses, 3 cycles). The membranes were subsequently solubilized by the addition of 1% (w/v) lauryl maltose neopentyl glycol (LMNG, Anatrace), followed by gentle agitation at 4 °C for 1 h. The solubilized lysate was cleared by centrifugation at 16,000 × *g* for 30 min to remove insoluble material. The supernatant was subsequently incubated with anti-FLAG M2 resin (Sigma-Aldrich) at 4 °C for 45 min with gentle agitation. The resin was then packed onto a gravity-flow column and washed with 10 column volumes of high-salt wash buffer (20 mM Tris pH 8, 300 mM NaCl, 5 mM ATP, 10 mM MgSO₄, 0.005% LMNG), followed by 10 column volumes of wash buffer (20 mM Tris pH 8, 150 mM NaCl, 0.005% LMNG). Protein was then eluted with 5 column volumes of elution buffer (20 mM Tris pH 8, 150 mM NaCl, 0.005% LMNG, 200 μg mL⁻¹ FLAG peptide). The eluted protein was concentrated with a 100 kDa-cutoff spin concentrator (Millipore), after which 1:10 (w/w) PreScission protease was added to the eluted protein and incubated at 4 °C for 1 h to cleave C-terminal tags. The mixture was further purified by injecting it onto a Superdex 200 Increase (Cytiva) size-exclusion column equilibrated with GF buffer (20 mM Tris pH 8, 150 mM NaCl, 0.005% LMNG). The peak fractions were pooled and concentrated for cryo-EM sample preparation.

Cryo-EM sample preparation

The peak fractions from final size-exclusion chromatography were concentrated to 9–10 mg ml⁻¹. For the no ligand added URAT1_{CS} sample, a final concentration of 2% DMSO was added. For ligand added samples (BBR-URAT1_{CS}, LESU-URAT1_{CS}, TD-3-URAT1_{CS}), 1 mM benz-bromarone, lesinurad (Sigma-Aldrich) or TD-3 dissolved in DMSO was added 30–40 min prior to vitrification. For no ligand added URAT1_{CS} and BBR-URAT1_{CS} samples, protein samples were mixed with a final concentration of 0.5 mM fluorinated octyl maltoside (FOM, Anatrace) prior to vitrification. For les-URAT1_{CS} and TD-3-URAT1_{CS} samples, protein samples were mixed with a final concentration of 0.25 mM FOM prior to vitrification. After mixing with FOM, 3 μL of sample was rapidly applied to a freshly glow-discharged UltrAuFoil RL2/1.3 300 mesh grids (Quantifoil), blotted with Whatman No. 1 filter paper for 1–1.5 s, then plunge-frozen in liquid-ethane cooled by liquid nitrogen.

Cryo-EM data collection

All datasets were collected using a Titan Krios (ThermoFisher) transmission electron microscope operating at 300 kV equipped with a K3 (Gatan) detector in counting mode behind a BioQuantum GIF energy filter with slit width of 20 eV. For no ligand added URAT1_{CS}, movies were collected at a nominal magnification of ×105,000 with a pixel size of 0.835 Å/px at specimen level, using Latitude S (Gatan) single particle data acquisition program. Each movie was acquired with a nominal dose rate of 19.2 e⁻/px/s over 1.8 s exposure time, resulting a total dose of -50 e⁻/Å² over 40 frames. The nominal defocus range was set from -0.7 to -1.7 μm.

BBR-URAT1_{CS} movies were collected at a nominal magnification of ×105,000 with a pixel size of 0.855 Å/px at specimen level using Latitude S. Each movie was acquired with a nominal dose rate of 19.3 e⁻/px/s over 2.0 s exposure time, resulting a total dose of -50 e⁻/Å² over 40 frames. The nominal defocus range was set from -0.8 to -1.8 μm.

Les-URAT1_{CS} dataset was collected using at a nominal magnification of ×105,000 with a super-resolution pixel size of 0.4128 Å/px at specimen level, using SerialEM⁵⁰ data acquisition program. Each movie was acquired with a nominal dose rate of 12.3 e⁻/px/s over 2.0 s exposure time, resulting a total dose of -45 e⁻/Å² over 45 frames. The nominal defocus range was set from -1.0 to -2.0 μm.

TD-3-URAT1_{CS} dataset was collected using at a nominal magnification of ×105,000 with a pixel size of 0.847 Å/px at specimen level, using SerialEM⁵⁰. Each movie was acquired with a nominal dose rate of 18.2 e⁻/px/s over 2.4 s exposure time, resulting a total dose of -60 e⁻/Å² and 60 frames. The nominal defocus range was set from -1.0 to -2.0 μm.

Cryo-EM data processing

No ligand added URAT1_{CS}. Beam-induced motion correction and dose-weighting for a total of 18,880 movies were performed using RELION 4.0⁵¹. Contrast transfer function parameters were estimated using cryoSPARC's patch CTF estimation⁵². Micrographs showing <4.5 Å estimated CTF resolution were discarded, leaving 18,854 micrographs. A subset of 1500 micrographs was used for blob picking in cryoSPARC⁵², followed by 2D classification to generate templates for template-based particle picking. 2D classes and associated particles that show the best secondary structure features were used to train a model in Topaz⁵³, which were subsequently used for particle picking with Topaz. A total of 6.98 million particles were picked, followed by particle extraction with a 64-pixel box size with 4× binning factor. A reference-free 2D classification was performed to remove obvious junk classes, resulting in a particle set of 6.08 million particles. An iterative ab initio reconstruction triplicate procedure was performed in cryoSPARC, as described previously^{19,54}. Four rounds of ab-initio triplicate runs were performed at 4× binned data, resulting in 4.04 million particles. The particles were then re-extracted with a 4× binned factor, and 6 rounds of ab-initio triplicates were performed, followed by re-extraction without a binning factor, at a 256-pixel box size and 2.49 million particles. Twenty-six rounds of ab-initio triplicates were performed with an unbinned particle set, which resulted in a 527,705 particle set and 3.33 Å resolution reconstruction by non-uniform refinement, and 3.05 Å resolution reconstruction by local refinement with a tight mask covering only the protein region. The particle is then transferred to RELION for Bayesian polishing, followed by transferring back to cryoSPARC for local refinement, resulting in a 2.68 Å final reconstruction with 527,705 particles.

BBR-URAT1_{CS}

Benz-URAT1_{CS} dataset was processed similarly to that for the no ligand added dataset with minor modifications. Beam-induced motion correction and dose-weighting for a total of 24,488 movies were performed using RELION 4.0⁵¹. Contrast transfer function parameters were estimated using cryoSPARC's patch CTF estimation⁵². Micrographs showing less than 4.5 Å estimated CTF resolution were discarded, leaving 21,879 micrographs. A subset of 1000 images was randomly selected for blob picking, which generated templates for template picking in cryoSPARC, followed by the generation of a 21k particle set for Topaz training. Using Topaz, a 7.73 million particle set was picked. After 2D classification clean-up, 5.50 million particles were retained and subjected to ab-initio triplicate runs. In brief, four, four and 39 rounds of ab-initio triplicate runs were performed at 4× binning, 2× binning and unbinned data sequentially, generating a particle set of 220,530 particles and a 3.29 Å reconstruction by non-uniform refinement. A tight mask covering only the protein region was generated using this map, and a local refinement using the same particle set and tight mask generated a 3.28 Å reconstruction. The particle set was then transferred to RELION for Bayesian polishing, then transferred back to cryoSPARC for non-uniform refinement and local refinements, yielding the final reconstruction of 3.0 Å with 220,530 particles.

LESU-URAT1_{CS}

Les-URAT1_{CS} dataset was processed similarly to that for the no ligand added dataset with minor modifications. Beam-induced motion correction and dose-weighting for a total of 13,746 movies were performed using RELION 4.0⁵¹. During motion correction, the micrographs were two times Fourier binned to generate micrographs with 0.8256 Å/px pixel size. Contrast transfer function parameters were estimated using cryoSPARC's patch CTF estimation⁵². Micrographs showing <4.0 Å estimated CTF resolution were discarded, leaving 13,320 micrographs. A subset of 1000 images was randomly selected for blob picking, which was used to generate templates for template picking in cryoSPARC, followed by the generation of a 32k particle set for Topaz

training. Subsequently, a 9.51 million particle set was picked using the trained Topaz model. After two rounds of 2D classification clean-up, 5.04 million particles were retained and subjected to ab-initio triplicate runs. In brief, four, seven and 21 rounds of ab-initio triplicate runs were performed at 4× binning, 2× binning and unbinned data sequentially, yielding a particle set of 512,313 particles and a 3.3 Å reconstruction by non-uniform refinement. The particle set was then transferred to RELION for Bayesian polishing, then transferred back to cryoSPARC for non-uniform refinement and local refinements, with the tight mask applied, generating the final reconstruction of 2.74 Å with 512,313 particles.

TD-3-URAT1_{CS}

TD-3-URAT1_{CS} dataset was processed similarly to that for the no ligand added dataset with minor modifications. Beam-induced motion correction and dose-weighting for a total of 19,122 movies were performed using RELION 4.0⁵¹. Contrast transfer function parameters were estimated using cryoSPARC's patch CTF estimation⁵². Micrographs showing less than 4.5 Å estimated CTF resolution were discarded, leaving 15,790 micrographs. A subset of 500 images was randomly selected for blob picking, which was used to generate templates for template picking in cryoSPARC, followed by the generation of a 56k particle set for Topaz training. Subsequently, a 1.95 million particle set was picked using the trained Topaz model. After 2D classification clean-up, 1.65 million particles were retained and subjected to ab-initio triplicate runs. In brief, three and four rounds of ab-initio triplicate runs were performed at 4× binning, 2× binning, respectively, yielding a particle set of 1.04 million particles and a 3.3 Å reconstruction by non-uniform refinement. Followed by ab-initio triplicate runs, two rounds of heterogeneous refinement were carried out, using three reference classes of the previously obtained 3.3 Å reconstruction without low-pass filtering, low-pass filtered to 6 Å and 10 Å, respectively. The class that shows the most prominent high-resolution features, containing 505,651 particles, was selected and subjected to non-uniform refinement and local refinement with tight masking, yielding a 2.73 Å reconstruction. The particles were then transferred to RELION for Bayesian polishing, then transferred back to cryoSPARC for local refinement, generating a final map of 2.55 Å.

Model building and refinement

All manual model building was performed in Coot⁵⁵ with ideal geometry restraints. A previous OCT1 model (PDB ID 8ET6) was used as an initial reference, followed by further manual model building and adjustment. Idealized CIF restraints for ligands were generated in eLBOW (in PHENIX software suite⁵⁶) from isomeric SMILES strings. After placement, manual adjustments were performed for both protein and ligands, ensuring correct stereochemistry and good geometries. The manually refined coordinates were subjected to real space refinement in phenix-real.space.refine in PHENIX with global minimization, local grid search and secondary structure restraints. MolProbity⁵⁷ was used to help identify errors and problematic regions. The refined TD-3-URAT1_{CS} cryo-EM structure was then rigid-body fit into the no ligand added URAT1_{CS}, BBR-URAT1_{CS} and LESU-URAT1_{CS} maps, followed by manual coordinate adjustments, ligand placement and adjustments, followed by phenix-real.space.refine in PHENIX. The Fourier shell correlation of the half- and full-maps against the model, calculated in PHENIX, was in good agreement for all four structures, indicating that the models did not suffer from over-refinement. Structural analysis and illustrations were performed using Open Source PyMOL and UCSF Chimera X⁵⁸.

MDs simulations

All-atom MD simulations in explicit solvents and POPC bilayer membranes were performed using the cryo-EM BBR-, LESU-, and TD-3-URAT1_{CS} structures. The systems were assembled using CHARMM-GUI Membrane Builder^{59,60}. Each system was solvated in TIP3P water and

neutralized with 0.15 M Na⁺ and Cl⁻ ions⁶¹. Five independent replicates were simulated for each system. Long-range electrostatics in solution were treated with the Particle-mesh Ewald summation^{62,63}, and van der Waals interactions were calculated with a cutoff distance of 9.0 Å. The systems were equilibrated following the CHARMM-GUI Membrane Builder protocol. The production runs were performed in the NPT (constant particle number, pressure, and temperature) for 1 μs at 303.15 K and 1 bar with hydrogen mass repartitioning^{64,65} using the following force fields: ff19SB for protein⁶⁶, OpenFF for ligand, and Lipid21 for lipid⁶⁷. All simulations were performed with the AMBER22 package⁶⁸ using the system inputs generated by CHARMM-GUI. Ligand binding stability was evaluated by calculating ligand RMSDs after superimposing the TM of the protein structure throughout the MD trajectory using CPPTRAJ⁶⁹.

Reporting summary

Further information on research design is available in the Nature Portfolio Reporting Summary linked to this article.

Data availability

The atomic coordinates have been deposited in the Protein Data Bank (PDB) under accession codes 9DK9 (no ligand added-URAT1_{CS}); 9DKA (BBR-URAT1_{CS}); 9DKB (LESU-URAT1_{CS}); and 9DKC (TD-3-URAT1_{CS}). The cryo-EM maps have been deposited in the Electron Microscopy Data Bank (EMDB) under accession codes EMD-46948 (no ligand added-URAT1_{CS}); EMD-46949 (BBR-URAT1_{CS}); EMD-46950 (LESU-URAT1_{CS}); and EMD-46951 (TD-3-URAT1_{CS}), respectively. The MD simulation data generated in this study have been deposited in Zenodo [<https://doi.org/10.5281/zenodo.15256013>]. We have used the following published structures for the initial model building: 8ET6. Source data are provided with this paper.

References

1. Dehlin, M., Jacobsson, L. & Roddy, E. Global epidemiology of gout: prevalence, incidence, treatment patterns and risk factors. *Nat. Rev. Rheumatol.* **16**, 380–390 (2020).
2. Punjwani, S. et al. Burden of gout among different WHO regions, 1990–2019: estimates from the global burden of disease study. *Sci. Rep.* **14**, 15953 (2024).
3. Skocznińska, M. et al. Pathophysiology of hyperuricemia and its clinical significance—a narrative review. *Reumatologia* **58**, 312–323 (2020).
4. Du, L. et al. Hyperuricemia and its related diseases: mechanisms and advances in therapy. *Signal Transduct. Target. Ther.* **9**, 212 (2024).
5. Li, X. et al. Serum uric acid levels and multiple health outcomes: umbrella review of evidence from observational studies, randomised controlled trials, and Mendelian randomisation studies. *BMJ* **357**, j2376 (2017).
6. Sharma, G., Dubey, A., Nolkha, N. & Singh, J. A. Hyperuricemia, urate-lowering therapy, and kidney outcomes: a systematic review and meta-analysis. *Ther. Adv. Musculoskelet. Dis.* **13**, 1759720X211016661 (2021).
7. Yu, Y. et al. Assessing the health risk of hyperuricemia in participants with persistent organic pollutants exposure—a systematic review and meta-analysis. *Ecotoxicol. Environ. Saf.* **251**, 114525 (2023).
8. Gu, T. et al. A systematic review and meta-analysis of the hyperuricemia risk from certain metals. *Clin. Rheumatol.* **41**, 3641–3660 (2022).
9. Enomoto, A. et al. Molecular identification of a renal urate-anion exchanger that regulates blood urate levels. *Nature* **417**, 447–452 (2002).
10. Xu, L., Shi, Y., Zhuang, S. & Liu, N. Recent advances on uric acid transporters. *Oncotarget* **8**, 100852 (2017).

11. Song, D., Zhao, X., Wang, F. & Wang, G. A brief review of urate transporter 1 (URAT1) inhibitors for the treatment of hyperuricemia and gout: current therapeutic options and potential applications. *Eur. J. Pharmacol.* **907**, 174291 (2021).
12. Chen, Y., You, R., Wang, K. & Wang, Y. Recent updates of natural and synthetic URAT1 inhibitors and novel screening methods. *Evid.-Based Complement. Alternat. Med.* **2021**, 5738900 (2021).
13. Nian, Y.-L. & You, C.-G. Susceptibility genes of hyperuricemia and gout. *Hereditas* **159**, 30 (2022).
14. Azevedo, V. F., Kos, I. A., Vargas-Santos, A. B., Pinheiro, G. D. R. C. & Paiva, E. D. S. Benzbromarone in the treatment of gout. *Adv. Rheumatol.* **59**, 37 (2019).
15. Jansen, T. T. A., Reinders, M., Van Roon, E. & Brouwers, J. Benzbromarone withdrawn from the European market: another case of “absence of evidence is evidence of absence”? [1]. *Clin. Exp. Rheumatol.* **22**, 651 (2004).
16. Zhang, M.-Y., Niu, J.-Q., Wen, X.-Y. & Jin, Q.-L. Liver failure associated with benzbromarone: a case report and review of the literature. *World J. Clin. Cases* **7**, 1717 (2019).
17. Deeks, E. D. Lesinurad: a review in hyperuricaemia of gout. *Drugs Aging* **34**, 401–410 (2017).
18. Zhao, T. et al. Discovery of novel bicyclic imidazolopyridine-containing human urate transporter 1 inhibitors as hypouricemic drug candidates with improved efficacy and favorable druggability. *J. Med. Chem.* **65**, 4218–4237 (2022).
19. Suo, Y. et al. Molecular basis of polyspecific drug and xenobiotic recognition by OCT1 and OCT2. *Nat. Struct. Mol. Biol.* **30**, 1001–1011 (2023).
20. Dou, T., Lian, T., Shu, S., He, Y. & Jiang, J. The substrate and inhibitor binding mechanism of polyspecific transporter OAT1 revealed by high-resolution cryo-EM. *Nat. Struct. Mol. Biol.* **30**, 1794–1805 (2023).
21. Parker, J. L., Kato, T., Kuteyi, G., Sitsel, O. & Newstead, S. Molecular basis for selective uptake and elimination of organic anions in the kidney by OAT1. *Nat. Struct. Mol. Biol.* **30**, 1786–1793 (2023).
22. Khanppnavar, B. et al. Structural basis of organic cation transporter-3 inhibition. *Nat. Commun.* **13**, 6714 (2022).
23. Dai, Y. & Lee, C.-H. Transport mechanism and structural pharmacology of human urate transporter URAT1. *Cell Res.* **34**, 776–787 (2024).
24. Niu, Y. et al. Structural basis of inhibition of the human SGLT2–MAP17 glucose transporter. *Nature* **601**, 280–284 (2022).
25. Wu, D. et al. Transport and inhibition mechanisms of human VMAT2. *Nature* **626**, 427–434 (2024).
26. Li, Y. et al. Dopamine reuptake and inhibitory mechanisms in human dopamine transporter. *Nature* **632**, 686–694 (2024).
27. Wright, N. J. & Lee, S.-Y. Structures of human ENT1 in complex with adenosine reuptake inhibitors. *Nat. Struct. Mol. Biol.* **26**, 599–606 (2019).
28. He, J. et al. Structural basis for the transport and substrate selection of human urate transporter 1. *Cell Rep.* **43**, 114628 (2024).
29. Drew, D., North, R. A., Nagarathinam, K. & Tanabe, M. Structures and general transport mechanisms by the major facilitator superfamily (MFS). *Chem. Rev.* **121**, 5289–5335 (2021).
30. Locuson, C. W., Suzuki, H., Rettie, A. E. & Jones, J. P. Charge and substituent effects on affinity and metabolism of benzbromarone-based CYP2C19 inhibitors. *J. Med. Chem.* **47**, 6768–6776 (2004).
31. Wu, C. et al. Molecular mechanisms of uric acid transport by the native human URAT1 and its inhibition by anti-gout drugs. *Cell Discov.* **11**, 33 (2024).
32. Suo, Y. et al. Structural insights into electrophile irritant sensing by the human TRPA1 channel. *Neuron* **105**, 882–894.e885 (2020).
33. Ringer, A. L., Senenko, A. & Sherrill, C. D. Models of S/π interactions in protein structures: comparison of the H2S–benzene complex with PDB data. *Protein Sci.* **16**, 2216–2223 (2007).
34. Hu, T. et al. Transport and inhibition mechanisms of the human noradrenaline transporter. *Nature* **632**, 930–937 (2024).
35. Yin, Y. et al. Mechanisms of sensory adaptation and inhibition of the cold and menthol receptor TRPM8. *Sci. Adv.* **10**, eadp2211 (2024).
36. Afek, A. et al. DNA mismatches reveal conformational penalties in protein–DNA recognition. *Nature* **587**, 291–296 (2020).
37. Lee, S.-Y. & MacKinnon, R. A membrane-access mechanism of ion channel inhibition by voltage sensor toxins from spider venom. *Nature* **430**, 232–235 (2004).
38. Cheng, T. et al. Computation of octanol–water partition coefficients by guiding an additive model with knowledge. *J. Chem. Inf. Model.* **47**, 2140–2148 (2007).
39. Gao, J. et al. A novel role of uricosuric agent benzbromarone in BK channel activation and reduction of airway smooth muscle contraction. *Mol. Pharmacol.* **103**, 241–254 (2023).
40. Huang, F. et al. Calcium-activated chloride channel TMEM16A modulates mucin secretion and airway smooth muscle contraction. *Proc. Natl Acad. Sci.* **109**, 16354–16359 (2012).
41. Zheng, Y. et al. Activation of peripheral KCNQ channels relieves gout pain. *Pain* **156**, 1025–1035 (2015).
42. Tang, L. W. T. et al. Differential reversible and irreversible interactions between benzbromarone and human cytochrome P450s 3A4 and 3A5. *Mol. Pharmacol.* **100**, 224–236 (2021).
43. Cotrina, E. Y. et al. Repurposing benzbromarone for familial amyloid polyneuropathy: a new transthyretin tetramer stabilizer. *Int. J. Mol. Sci.* **21**, 7166 (2020).
44. Cai, H.-y et al. Benzbromarone, an old uricosuric drug, inhibits human fatty acid binding protein 4 in vitro and lowers the blood glucose level in db/db mice. *Acta Pharmacol. Sin.* **34**, 1397–1402 (2013).
45. Loo, T. W., Bartlett, M. C. & Clarke, D. M. Benzbromarone stabilizes ΔF508 CFTR at the cell surface. *Biochemistry* **50**, 4393–4395 (2011).
46. Katoh, K. & Toh, H. Recent developments in the MAFFT multiple sequence alignment program. *Brief. Bioinformatics* **9**, 286–298 (2008).
47. Waterhouse, A. M., Procter, J. B., Martin, D. M., Clamp, M. & Barton, G. J. Jalview version 2—a multiple sequence alignment editor and analysis workbench. *Bioinformatics* **25**, 1189–1191 (2009).
48. Tan, P. K., Ostertag, T. M. & Miner, J. N. Mechanism of high-affinity inhibition of the human urate transporter URAT1. *Sci. Rep.* **6**, 34995 (2016).
49. Cornish-Bowden, A. *Fundamentals of enzyme kinetics*. (John Wiley & Sons, 2013).
50. Mastronarde, D. N. SerialEM: a program for automated tilt series acquisition on Tecnai microscopes using prediction of specimen position. *Microsc. Microanal.* **9**, 1182–1183 (2003).
51. Zivanov, J. et al. A Bayesian approach to single-particle electron cryo-tomography in RELION-4.0. *Elife* **11**, e83724 (2022).
52. Punjani, A., Rubinstein, J. L., Fleet, D. J. & Brubaker, M. A. cryoSPARC: algorithms for rapid unsupervised cryo-EM structure determination. *Nat. Methods* **14**, 290–296 (2017).
53. Bepler, T. et al. Positive-unlabeled convolutional neural networks for particle picking in cryo-electron micrographs. *Nat. Methods* **16**, 1153–1160 (2019).
54. Wright, N. J. et al. Methotrexate recognition by the human reduced folate carrier SLC19A1. *Nature* **609**, 1056–1062 (2022).
55. Emsley, P., Lohkamp, B., Scott, W. G. & Cowtan, K. Features and development of coot. *Acta Crystallogr. Sect. D: Biol. Crystallogr.* **66**, 486–501 (2010).
56. Liebschner, D. et al. Macromolecular structure determination using X-rays, neutrons and electrons: recent developments in Phenix. *Acta Crystallogr. Sect. D: Struct. Biol.* **75**, 861–877 (2019).
57. Williams, C. J. et al. MolProbity: more and better reference data for improved all-atom structure validation. *Protein Sci.* **27**, 293–315 (2018).

58. Meng, E. C. et al. UCSF ChimeraX: tools for structure building and analysis. *Protein Sci.* **32**, e4792 (2023).
59. Jo, S., Kim, T., Iyer, V. G. & Im, W. CHARMM-GUI: a web-based graphical user interface for CHARMM. *J. Comput. Chem.* **29**, 1859–1865 (2008).
60. Lee, J. et al. CHARMM-GUI membrane builder for complex biological membrane simulations with glycolipids and lipoglycans. *J. Chem. Theory Comput.* **15**, 775–786 (2019).
61. Jorgensen, W. L., Chandrasekhar, J., Madura, J. D., Impey, R. W. & Klein, M. L. Comparison of simple potential functions for simulating liquid water. *J. Chem. Phys.* **79**, 926–935 (1983).
62. Darden, T., York, D. & Pedersen, L. Particle Mesh Ewald - an N.Log(N) method for Ewald sums in large systems. *J. Chem. Phys.* **98**, 10089–10092 (1993).
63. Essmann, U. et al. A smooth particle mesh Ewald method. *J. Chem. Phys.* **103**, 8577–8593 (1995).
64. Hopkins, C. W., Le Grand, S., Walker, R. C. & Roitberg, A. E. Long-time-step molecular dynamics through hydrogen mass repartitioning. *J. Chem. Theory Comput.* **11**, 1864–1874 (2015).
65. Gao, Y. et al. CHARMM-GUI supports hydrogen mass repartitioning and different protonation states of phosphates in lipopolysaccharides. *J. Chem. Inf. Model.* **61**, 831–839 (2021).
66. Tian, C. et al. ff19SB: amino-acid-specific protein backbone parameters trained against quantum mechanics energy surfaces in solution. *J. Chem. Theory Comput.* **16**, 528–552 (2020).
67. Dickson, C. J., Walker, R. C. & Gould, I. R. Lipid21: complex lipid membrane simulations with AMBER. *J. Chem. Theory Comput.* **18**, 1726–1736 (2022).
68. Case, D. A. et al. AmberTools. *J. Chem. Inf. Model.* **63**, 6183–6191 (2023).
69. Roe, D. R. & Cheatham, T. E. 3rd. PTRAJ and CPPTRAJ: software for processing and analysis of molecular dynamics trajectory data. *J. Chem. Theory Comput.* **9**, 3084–3095 (2013).
- Research Triangle Nanotechnology Network, which is in part supported by the NSF (ECCS-2025064).

Author contributions

Y.S. and J.G.F. conducted all single-particle 3D cryo-EM reconstruction and biochemical experiments. H.Z. and S.K. carried out all MD simulations under the guidance of W.L., X.S. synthesized TD-3 under the guidance of P.Z., K.S. screened and collected part of the data under the guidance of M.B., S.-Y.L., and Y.S. performed model building and refinement. K.T. did preliminary biochemical experiments. Y.S., J.G.F., and S.-Y.L. wrote the paper.

Competing interests

The authors declare no competing interests.

Additional information

Supplementary information The online version contains supplementary material available at <https://doi.org/10.1038/s41467-025-60480-3>.

Correspondence and requests for materials should be addressed to Seok-Yong Lee.

Peer review information *Nature Communications* thanks the anonymous reviewers for their contribution to the peer review of this work. A peer review file is available.

Reprints and permissions information is available at <http://www.nature.com/reprints>

Publisher's note Springer Nature remains neutral with regard to jurisdictional claims in published maps and institutional affiliations.

Open Access This article is licensed under a Creative Commons Attribution-NonCommercial-NoDerivatives 4.0 International License, which permits any non-commercial use, sharing, distribution and reproduction in any medium or format, as long as you give appropriate credit to the original author(s) and the source, provide a link to the Creative Commons licence, and indicate if you modified the licensed material. You do not have permission under this licence to share adapted material derived from this article or parts of it. The images or other third party material in this article are included in the article's Creative Commons licence, unless indicated otherwise in a credit line to the material. If material is not included in the article's Creative Commons licence and your intended use is not permitted by statutory regulation or exceeds the permitted use, you will need to obtain permission directly from the copyright holder. To view a copy of this licence, visit <http://creativecommons.org/licenses/by-nc-nd/4.0/>.

© The Author(s) 2025

Acknowledgements

Cryo-EM data were screened and collected at the National Institute of Environmental Health Sciences cryo-EM facility and Duke University Shared Materials Instrumentation Facility, Pacific National Cryo-EM Center (PNCC) and National Cryo-EM Facility (NCEF). We thank Nilakshee Bhattacharya at SMIF, Janette Myers at PNCC and Tara Fox at NCEF for assistance with the microscope operation. This research was supported by Duke Science Technology Scholar Funds (S.-Y.L.). We thank Nicholas Wright for valuable advice on this project and Zhenning Ren for critical reading of the manuscript. A portion of this research was supported by the National Institute of Health Intramural Research Program; US National Institutes of Environmental Health Sciences (ZIC ES103326 to M.J.B.), the National Cancer Institute's National Cryo-EM Facility at the Frederick National Laboratory for Cancer Research under contract 75N91019D00024, by the NIH grant U24GM129547 and performed at the PNCC at OHSU and accessed through EMSL (grid.436923.9), a DOE Office of Science User Facility sponsored by the Office of Biological and Environmental Research. DUKE SMIF is affiliated with the North Carolina